High-*n* limit of quantum defects for high-ℓ strontium Rydberg states

G. Fields,[1] R. Brienza,[1] F. B. Dunning,[1] S. Yoshida ◉,[2] and J. Burgdörfer[2]

[1]*Department of Physics and Astronomy, Rice University, Houston, Texas 77005-1892, USA*
[2]*Institute for Theoretical Physics, Vienna University of Technology, 1040 Vienna, Austria, EU*

Studies of high-*n*, $120 \lesssim n \lesssim 160$, strontium $5sng$, $5snh$, and $5sni$ Rydberg states are reported. Measurements using microwave spectroscopy provide the quantum defects for these states and furnish a valuable test of quantum defects reported for lower-ℓ states in the high-*n* limit. With increasing ℓ the relativistic spin-orbit interaction becomes comparable to the electron-electron interaction resulting in the breakdown of the standard *LS*-coupling scheme. Heavier alkaline-earth quasi-two-electron systems differ significantly from a true two-electron system such as helium because indirect spin-orbit effects are dramatically enhanced. We explore the high-*n* limit of this transition between *LS* and *jj* coupling. For high-ℓ states the quantum defects are determined predominantly by the polarizability of the inner electrons.

I. INTRODUCTION

The production of high-ℓ, $\ell > 3$, Rydberg atoms enables several new avenues of study. One prominent example is the formation of ultralong-range molecules in "trilobite" states which, in contrast to typical homonuclear dimers, have large permanent electric dipole moments [1–3]. These novel molecules can be formed because of the near degeneracy of high-ℓ states. Another new avenue specific to strontium Rydberg atoms, which are the focus of this study, takes advantage of the fact the core ion has convenient $5s \rightarrow 5p_{1/2,3/2}$ optical transitions that have been exploited to cool strontium plasmas [4]. In principle, the same transitions in the core ion of a Rydberg atom might be used to cool and trap Rydberg atoms or to image a cloud of Rydberg atoms provided core penetration can be made sufficiently small through use of high-ℓ (and high-*n*) states so as to suppress autoionization [5]. Furthermore, such suppression might allow creation of long-lived two-electron-excited planetary atoms [6–9].

For Rydberg atoms in high-ℓ levels ($4 \leqslant \ell \leqslant 7$) the interaction between the Rydberg and core electrons is typically small. The electronic structure of two-electron systems such as helium (or its isoelectronic partners) and quasi-two-electron systems such as alkaline-earth atoms is (primarily) governed by the pair interaction between the inner valence electron and the Rydberg electron. Because of the high centrifugal barrier separating the inner and the outer electrons, the orbits of the two electrons are spatially well separated, thereby suppressing the direct electron-electron interaction. Therefore, in helium, the magnetic spin-orbit coupling can become dominant. In particular, when the inner electron cloud is confined within the orbit of a high-ℓ Rydberg electron, the interaction of the spin of the inner electron with the magnetic field induced by the orbital motion of the outer electron becomes non-negligible. Such interactions can be described by the Breit-Bethe Hamiltonian [10] and cause the mixing

of singlet and triplet states, thereby signaling the breakdown of *LS* coupling. For heavier atoms (Sr, Ba, and Si^{2+}), measurements [11–13] show significantly larger energy splittings than those predicted by the Breit-Bethe Hamiltonian. This has been interpreted as due to the large dynamical polarizability of the inner electron with significant correlation between the inner valence electron and the Rydberg electron [13,14]. This high-ℓ limit is qualitatively similar to, but quantitatively significantly different from, alkali-metal atoms where the weak polarization of the closed-shell core plays an important role in determining the level structure of high angular momentum Rydberg states [15].

In the present work we examine, through the production of high-*n* ($120 \lesssim n \lesssim 160$) strontium (^{88}Sr) $5sn\ell$ ($3 \leqslant \ell \leqslant 5$) Rydberg states, the high-*n* behavior of the transition regime between where the electronic structure is dominated by electron-electron interactions and by spin-orbit interactions. Measurements of the energy levels and of the quantum defects δ for $3 \leqslant \ell \leqslant 6$ at low *n* ($\lesssim 40$) have been reported [13,16,17]. Here we extend this earlier work to significantly higher *n* and present measurements of the quantum defects for $5snf$, $5sng$, $5snh$, and $5sni$ states at higher *n*. For these high-ℓ states the mixing of singlet and triplet states caused by the spin-orbit coupling is analyzed theoretically using a quasi-two-electron model. The measurements demonstrate a splitting of the $5sng$ states indicating the mixing of singlet and triplet states. The theoretical analysis can be used to determine which of the observed Rydberg states should be described by the *LS*-coupling scheme and which by the *jj*-coupling scheme. The calculations reveal that core polarization plays an important role in determining the quantum defects for high-ℓ states, while core penetration by the Rydberg electron dominates for low-ℓ states. The asymptotic behavior of the quantum defects in the high-*n* limit is also discussed. In addition, the present work furnishes a test in the high-*n* limit of the published Rydberg-Ritz parametrization for the quantum
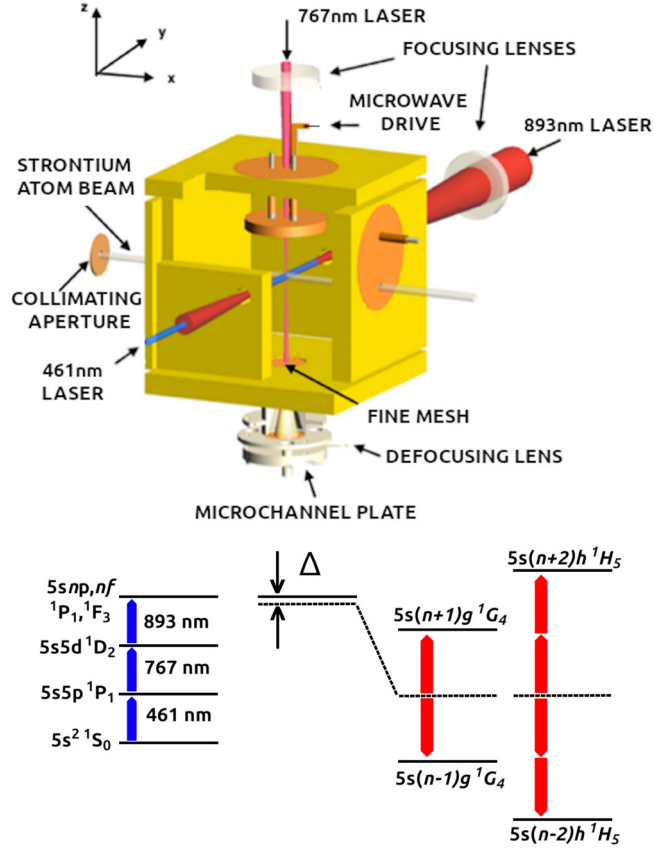
FIG. 1. Schematic diagram of the apparatus. The strontium energy levels and transitions important in the present work are also shown.

defects of lower-ℓ $^1P_1$ and $^1D_2$ states, which were (typically) derived from measurements at low n ($n \lesssim 50$) [18,19].

II. EXPERIMENTAL APPROACH

The Rydberg excitation schemes employed here are diagramed in Fig. 1. The first two lasers, operating at 461 and 767 nm, are tuned on resonance with the $5s^2\,^1S_0 \rightarrow 5s5p\,^1P_1$ and the $5s5p\,^1P_1 \rightarrow 5s5d\,^1D_2$ transitions, respectively. For production of $5snf\,^1F_3$ (and $5snp\,^1P_1$) states, the third laser, which operates at $\sim$893 nm, is tuned to the target state. Microwave radiation is then used to enable four- and five-photon microwave-optical excitation to the neighboring $5s(n \pm 1)g$ and $5s(n \pm 2)h$ Rydberg states. Sizable $5sng$ Rydberg production rates are facilitated by the large electric dipole matrix elements $\sim n^2$ (atomic units are used here unless otherwise noted) that couple transitions between Rydberg levels. The $5snh$ production rates achieved are smaller, but sufficient numbers of such states can be generated for their study.

The present apparatus, shown schematically in Fig. 1, has been described in detail previously [20]. Briefly, strontium atoms contained in an atomic beam are excited to Rydberg states using the excitation schemes indicated in the inset. The three crossed laser beams are focused to define a small excitation volume $\sim$70 μm on a side. The laser output frequencies are controlled with the aid of Fabry-Pérot étalons

that are stabilized using the output of a 689-nm laser that is locked to the strontium $5s^2\,^1S_0 \rightarrow 5s5p\,^3P_1$ transition using saturated absorption spectroscopy. The free spectral ranges of the étalons, $\sim$1.5 GHz, allow the lasers to be tuned with a resolution of $\sim \pm 2$ MHz and provide control of long-term drifts in their output frequencies to within similar limits. The 461- and 767-nm lasers are polarized in the vertical, i.e., z, direction (see Fig. 1) and the 893-nm IR laser is polarized in the y direction. Optical excitation alone therefore populates states with $M_J = \pm 1$. Excitation occurs at the center of an interaction region defined using three pairs of copper electrodes to which are applied small offset potentials to locally reduce the stray fields in the excitation volume. The required potentials are determined using a spectroscopic technique based on Stark energy-level shifts that is detailed elsewhere and which allows stray fields to be reduced to $\lesssim$50 μV cm^{-1} [21]. The microwave fields are generated by applying the output of a frequency synthesizer to a circular electrode positioned above the excitation volume. The input semirigid coaxial cable is terminated by a 50-Ω resistor at the electrode. (The synthesizer provides 10-kHz frequency steps and, tests revealed, is stable within this limit independent of output drive voltage.) The amplitudes of the microwave drive voltages applied to the electrode range from $\sim$100 to 0.1 mV and result in the production of relatively weak microwave fields. Application of a DC bias of 100 mV (0.1 mV) to the electrode results in a DC field of $\sim$15(0.015) mV cm^{-1} in the excitation region. In the present work, however, microwave frequencies of $\sim$2–4 GHz are employed. In consequence, retardation (and possibly resonance) effects become important and it is not possible to simply relate the strength of the microwave field generated in the excitation volume to the amplitude of the drive voltage. Nonetheless, it is reasonable to expect that, for a fixed microwave frequency, the applied microwave field should be proportional to the drive voltage amplitude. Furthermore, knowledge of the exact strength of the microwave field is not required in the present work.

Experiments are conducted in a pulsed mode. The output of the 461-nm IR laser used to excite the first optical transition is chopped into a train of pulses with durations of $\sim$1 μs and a pulse repetition frequency of $\sim$10 kHz using an acousto-optic modulator. The other two lasers remain on at all times but play no further role as Rydberg atoms, once created, rapidly exit the excitation region as a result of their thermal velocities. The microwave field is also pulsed. For spectroscopic studies of transitions from $5snf\,^1F_3$ levels the pulses are applied sequentially. The IR laser is first tuned to directly excite the desired initial $n\,^1F_3$ (or $n\,^1P_1$) Rydberg state whereupon, following a brief $\sim$100-ns delay, the microwave field is applied (typically for $\sim$1 μs) to excite transitions to neighboring Rydberg states. Rydberg atoms are detected, and their states analyzed, using selective field ionization (SFI). A linearly increasing electric field $F_{SFI}(t)$ is generated in the experimental volume by application of a voltage ramp to the bottom electrode that has a rise time of $\sim$4 μs. The product electrons are collected and directed through a series of grids to a dual microchannel plate detector whose output can be fed to either a multichannel scaler or a time-to-amplitude converter to determine the time, and hence field, at which ionization occurred. Selective field ionization spectra are
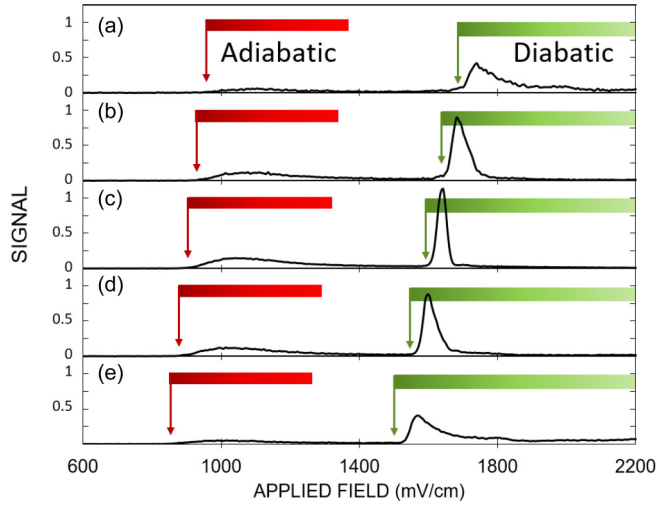
FIG. 2. SFI spectra recorded for (a) $5s135h_{9/2,11/2}$, (b) $5s136g_{7/2,9/2}$, (c) $5s137f\,^1F_3$, (d) $5s138g_{7/2,9/2}$, and (e) $5s139h_{9/2,11/2}$ states plotted as a function of applied field F_{SFI}. The horizontal bars denote the range of fields over which ionization along principally adiabatic (red) and principally diabatic (green) paths is expected. The threshold for adiabatic ionization, $\sim 1/(16n^4)$, corresponds to that for classical over-the-barrier ionization and that for diabatic ionization, $\sim 1/(9n^4)$, corresponds to purely diabatic ionization of the redmost Stark states.

built up by accumulating data following many experimental cycles.

When the high-ℓ states ($\ell > 3$) are excited from an adjacent $5snf\,^1F_3$ state using a microwave field, the product state is a coherent superposition of the initial F state and the target high-ℓ state. It is often challenging to identify the contributions from different ℓ levels in SFI. In the present experiments the microwaves are tuned to excite $5snf$ states to $5s(n\pm1)g$ or $5s(n\pm2)h$ states. Using this correlation between n and ℓ, the angular momentum ℓ of the product state can be indirectly measured by probing the principal quantum number n. Figure 2 shows SFI spectra recorded for a number of different angular momentum states with values of $n \sim 137$ plotted as a function of applied field. The $5s137f\,^1F_3$ state is excited by three optical photons, whereas the higher-ℓ states are created using combined microwave and optical photons (see Fig. 1). For the latter, the 893-mm IR laser was detuned by $\Delta = -30$ MHz from the transition to the $5s137f\,^1F_3$ state. The microwave and optical pulses are of equal duration and are applied concurrently. For nonhydrogenic atoms the interaction between the Rydberg electron and the core electrons forms avoided crossings in the level structure [22,23]. When the avoided crossings are traversed predominantly adiabatically as the applied field is increased, ionization occurs near a threshold field F_a which, for high-ℓ states, is given approximately by $1/(16n^4)$ and, when traversed principally diabatically, near a threshold field $F_d \sim 1/(9n^4)$. Which behavior occurs depends sensitively on the size of the energy spacings at avoided crossings, which in turn depend on the principal quantum number n and the magnetic quantum number m (relative to the quantization axis defined by the ionizing field), as well as on the slew rate of the applied field. The

horizontal bars in Fig. 2 indicate the ranges of field over which ionization is expected if ionization proceeds adiabatically and diabatically towards the respective ionization thresholds. For the present electric field slew rate, $\sim 1.2 \times 10^6$ V cm^{-1} s^{-1}, the SFI spectrum for the $137\,^1F_3$ state exhibits a broad feature around the adiabatic threshold and a sharp peak near the diabatic threshold. This narrow peak can be used to identify the principal quantum number n of the product state. The counterparts for the higher-ℓ ($\ell = 4, 5$) states have relatively small overlaps with the narrow peak of the $137\,^1F_3$ state due to the shift of the ionization thresholds to $1/[9(n\pm1)^4]$ or $1/[9(n\pm2)^4]$. These shifts are large enough to identify the different n levels or, equivalently, the different final ℓ levels. The broadened peaks for high-ℓ ($\ell = 4, 5$) states are due in part to the relatively large microwave drive voltages applied to obtain sizable excitation probabilities given the large detuning of the 893-nm laser from the $5s137f\,^1F_3$ level. Consequently, the product state is very likely a dressed state involving a small admixture of states from adjacent n levels which broadens the peak near the diabatic threshold. In the present spectroscopic studies, however, only very small microwave voltages are required to drive transitions from the initial $^1F_3$ states to the higher-ℓ states, which limits any similar broadening of their associated diabatic features in the SFI spectra, thereby allowing different ℓ levels to be more clearly identified.

III. STRUCTURE OF HIGH-ℓ RYDBERG STATES

Due to the magnetic fine structure, the excitation spectrum of a high-ℓ Rydberg state $5sn\ell$ can show an energy-level splitting. In the transition regime between LS and jj coupling, in particular, the level structure needs to be analyzed to identify which Rydberg state is observed in the measured excitation spectra. In this section we analyze theoretically the level structures of high-ℓ Rydberg states of strontium. In Sec. IV the measured spectra are analyzed using these theoretical predictions.

The singly-excited Rydberg states of strontium can be treated as a quasi-two-electron problem with the krypton-like closed-shell core providing an effective central potential $V_c(r)$. Accordingly, the Hamiltonian of this quasi-two-electron system including lowest-order relativistic spin-orbit and spin-spin corrections to order α^2 (α is the fine-structure constant) is given by [24]

$$H = \sum_{i=1}^{2}\left(\frac{p_i^2}{2} + V_c(r_i) + V_{\text{so}}(r_i)\right) + V_{ee}, \qquad (1)$$

with

$$V_{\text{so}}(r) = \frac{\alpha^2}{2}(\vec{\ell}\cdot\vec{s})\frac{1}{r}\frac{dV_c(r)}{dr} \qquad (2)$$

the standard Pauli one-electron spin-orbit interaction and V_{ee} the electron-electron interaction

$$V_{ee} = \frac{1}{|\vec{r}_1 - \vec{r}_2|} - \frac{\alpha^2}{|\vec{r}_1 - \vec{r}_2|^3}(\vec{\ell}_1\cdot\vec{s}_2 + \vec{\ell}_2\cdot\vec{s}_1)$$
$$+ \alpha^2\frac{\vec{s}_1\cdot\vec{s}_2 - 3(\vec{s}_1\cdot\hat{r}_{12})(\vec{s}_2\cdot\hat{r}_{12})}{|\vec{r}_1 - \vec{r}_2|^3} \qquad (3)$$

containing the electrostatic Coulomb interaction $1/|\vec{r}_1 - \vec{r}_2|$ and the magnetic interaction of the Breit-Bethe spin Hamiltonian. In the present case where one electron is in a high-ℓ Rydberg state only the spin-orbit interaction of the inner valence (v) electron $V_{so}(r_v)$ [Eq. (2)] and (to some extent) the spin-outer orbital angular momentum term $\sim \vec{s}_v \cdot \vec{\ell}_R$, with $\vec{\ell}_R$ the angular momentum of the Rydberg electron, of the magnetic fine structure play a role. In general, the model potential for the core V_c depends on ℓ but is, in the present analysis, approximated by an ℓ-independent potential for $\ell \geqslant 3$. More details of the potentials $V_c(r)$ and $V_{so}(r)$ used for the present study can be found elsewhere [25,26].

The electronic structure of high-ℓ Rydberg states is determined by the competition between the interelectron Coulomb interaction and the spin-orbit interaction involving the spin of the inner electron. When the Coulomb interaction dominates, the total spin of the quasi-two-electron system $\vec{S} = \vec{s}_v + \vec{s}_R$ and the total angular momentum $\vec{L} = \vec{\ell}_v + \vec{\ell}_R$ are separately conserved and the Rydberg states are well represented by the *LS*-coupling scheme, i.e., $|(n_1\ell_1, n_2\ell_2)^{2S+1}L_J\rangle$ with the total angular momentum $\vec{J} = \vec{L} + \vec{S}$. With increasing ℓ_R, the (direct) electrostatic Coulomb interaction becomes suppressed as the increasingly high centrifugal barrier enforces the spatial separation and vanishing overlap between the valence electron ($\ell_v = 0$ for strontium) and the outer Rydberg electron. In this limit the spin-orbit interaction, in particular the one involving the spin of the valence electron, dominates and the Rydberg state is more accurately represented by the jj-coupling scheme, i.e., $|(n_1\ell_{j_1}, n_2\ell_{j_2})J\rangle$. The transformation between the two representations is given by the Wigner 9-j symbols [27]. In the special case of an inner s electron $\ell_v = 0$, the transformation matrix reduces to 6-j symbols [27]. In the present case of $s_v = s_R = \frac{1}{2}$, the two coupling schemes coincide for $J = \ell_R \pm 1$, while in the subspace $J = \ell_R$ the transformation $|(5s_{1/2}n\ell_j)J\rangle = O|(5sn\ell)^1L_J\rangle$ is given by a 2×2 rotation matrix

$$\begin{pmatrix} |(5s_{1/2}n\ell_{j=\ell+1/2})J=\ell\rangle \\ |(5s_{1/2}n\ell_{j=\ell-1/2})J=\ell\rangle \end{pmatrix}$$
$$= \begin{pmatrix} \cos\theta & -\sin\theta \\ \sin\theta & \cos\theta \end{pmatrix} \begin{pmatrix} |(5sn\ell)^1L_{J=L}\rangle \\ |(5sn\ell)^3L_{J=L}\rangle \end{pmatrix} \quad (4)$$

with $\theta = \tan^{-1}[\sqrt{\ell/(\ell+1)}]$. Since here and in the following $\ell_v = 0$ unless stated otherwise, we have simplified the notation in Eq. (4) to $\ell_R = \ell = L$. In the limit of $\ell \gg 1$, θ approaches $\pi/4$, resulting in an equal mixture of the singlet and the triplet character of the state. We note that, up to phase factors, for s states ($\ell_v = 0$) the transformation matrix O agrees with that for the transformation to the so-called intermediate coupling to an intermediate angular momentum K [13,14] that treats the spin of the inner and outer electron nonequivalently, $|(((\ell_v s_v)j_v \ell_R)Ks_R)J\rangle$. The latter is well suited when the spin-orbit interaction of the Rydberg electron can be neglected, giving rise to (near-)degenerate K doublets. In this nonequivalent description the valence and Rydberg electrons can be viewed as distinguishable.

The energy of a given Rydberg state is conventionally parametrized by its deviation from the hydrogenic limit $E_n =$ $-1/(2n^2)$ in terms of a quantum defect $\delta(n, \ell)$,

$$E = -\frac{1}{2(n - \delta(n, \ell))^2} \simeq E_n - \frac{\delta(n, \ell)}{n^3}. \quad (5)$$

Its dependence on ℓ for very large $n > 100$ and large ℓ will be explored in the following for strontium as a prototypical quasi-two-electron system.

As a point of reference, consider a similar analysis of quantum defects for high-ℓ alkali-metal atoms [15] which we take as being typical of quasi-one-electron systems. Here the contribution from the magnetic fine structure is negligible and the interaction of the spatially well separated Rydberg electron with the closed-shell core can be described in terms of multipolar polarizabilities

$$\delta \simeq \frac{n^3}{2}[\alpha_d \langle r^{-4}\rangle + \alpha_q \langle r^{-6}\rangle], \quad (6)$$

where α_d and α_q are the effective dipole and quadrupole polarizabilities of the core and $\langle r^{-k}\rangle$ is the expectation value of powers of the inverse distance of the Rydberg electron from the core evaluated by the wave function of the Rydberg electron. Using hydrogenic wave functions for the evaluation of the moments yields

$$n^3\langle r^{-4}\rangle = A_4[3 - n^{-2}\ell(\ell+1)] \quad (7)$$

with $A_4 = [2(\ell - \frac{1}{2})\ell(\ell + \frac{1}{2})(\ell + 1)(\ell + \frac{3}{2})]^{-1}$ and

$$n^3\langle r^{-6}\rangle = A_6[35 - 5n^{-2}(6\ell^2 + 6\ell - 5) + 3n^{-4}(\ell - 1)$$
$$\times \ell(\ell+1)(\ell+2)] \quad (8)$$

with $A_6 = A_4/[4(\ell - \frac{3}{2})(\ell - 1)(\ell + 2)(\ell + \frac{5}{2})]$. This leads to a Rydberg-Ritz-like formula for the quantum defect

$$\delta(n, \ell) = \delta_0(\ell) + \frac{\mu_2(\ell)}{n^2} + \frac{\mu_4(\ell)}{n^4} \quad (9)$$

with

$$\delta_0(\ell) = \frac{3}{2}A_4\alpha_d + \frac{35}{2}A_6\alpha_q, \quad (10a)$$

$$\mu_2(\ell) = -\frac{1}{2}[\ell(\ell+1)A_4\alpha_d + 5(6\ell^2 + 6\ell - 5)A_6\alpha_q], \quad (10b)$$

$$\mu_4(\ell) = \frac{3}{2}(\ell - 1)\ell(\ell + 1)(\ell + 2)A_6\alpha_q. \quad (10c)$$

In the high-n limit, therefore, the quantum defect is expected to converge to the asymptotic value δ_0 with leading corrections $\sim \mu_2/n^2$.

For alkaline-earth atoms the correlation between the Rydberg electron and the valence electron outside the closed core causes much stronger dynamical polarization effects and the competition between the spin-orbit interaction of the valence electron and the Rydberg-valence electron correlation determines the Rydberg spectrum and thus the quantum defect. With a multipole expansion of the electron-electron interaction [28] the Hamiltonian [Eq. (1)] can be rewritten as

$$H = H_0 + U = H_0 + \sum_{k=1}^{\infty} U_k(\vec{r}_1, \vec{r}_2), \quad (11)$$

with

$$H_0 = \sum_{i=v,R} \left(\frac{p_i^2}{2} + V_c(r_i) + V_{so}(r_i) \right) + \frac{1}{r_>} \quad (12)$$

and

$$U_k(\vec{r}_1, \vec{r}_2) = \sum_{m_k=-k}^{k} \left[\frac{r_<^k}{r_>^{k+1}} \frac{4\pi}{2k+1} Y_k^{m_k}(\theta_1, \phi_1) Y_k^{m_k*}(\theta_2, \phi_2) \right.$$
$$\left. - \delta_{k,1} \frac{\alpha^2}{r_R^3} \vec{s}_V \cdot \vec{\ell}_R \right]. \qquad (13)$$

The zeroth-order term $1/r_>$ of the electron-electron interaction is excluded from the perturbation U but included in the unperturbed Hamiltonian [Eq. (12)]. This term screens the potential $V_c(r)$ of the Sr^{2+} ion core facilitating the convergence to the Coulomb potential $V_c(r) + 1/r \simeq -1/r$ at large r. We include the spin-orbit interaction between the spin of the valence electron and the orbital angular momentum of the Rydberg electron in the dipole component ($k = 1$) of the multipole expansion of the perturbation U for completeness. While for helium Rydberg states this electron-electron magnetic dipole fine structure in the atom significantly contributes to the splitting [10], in alkaline-earth atoms it is overshadowed by the indirect interaction via the dynamical polarization induced by the electrostatic multipoles. Indeed, the spin-orbit interaction between the spin of the valence electron and the orbital angular momentum of the Rydberg electron is on the order of twice the spin-orbit coupling of the Rydberg electron $2V_{\text{so}}(r_R)$ and is smaller than the interaction induced by the dynamical polarization, for example, by a factor of $\frac{1}{83}$ for barium [14]. Finally, the direct spin-spin dipole interaction [Eq. (3)] can be safely neglected.

The resulting quantum defect for strontium high-ℓ Rydberg states

$$\delta(n, \ell) = n^3 \left(\Delta E_{n\ell_j}^{(0)} + \Delta E_{\text{ee}} \right) \qquad (14)$$

originates predominantly from two contributions. The first is the deviation of the eigenvalue of the unperturbed Hamiltonian H_0 [Eq. (12)],

$$H_0 |(5s_{1/2}n\ell_j)J\rangle_0 = E_{n\ell_j}^{(0)} |(5s_{1/2}n\ell_j)J\rangle_0, \qquad (15)$$

from its hydrogenic limit E_n,

$$\Delta E_{n\ell_j}^{(0)} = E_n - E_{n\ell_j}^{(0)}, \qquad (16)$$

which includes the residual penetration and fine structure built into the antisymmetrized eigenstates $|(5s_{1/2}n\ell_j)J\rangle_0$ of H_0 and is shown in Fig. 3(a). As expected, with increasing ℓ ($\ell \geqslant 3$) penetration of the Rydberg electron into the region of the $5s$ valence electron and, even more so, into the closed-shell core is rapidly suppressed. A second contribution to δ originates from the electron-electron interaction terms U [Eq. (11)]. The matrix elements of the electrostatic multipoles U_k [Eq. (13)] are diagonal in the LS basis but couple the states of the jj representation. For strontium the exchange energy to first order in U_k,

$$E_{\text{ex}}^{(1)}(n\ell_j) = {}_0\langle(5s_{1/2}n\ell_j)J|U_{k=\ell}|(5s_{1/2}n\ell_j)J\rangle_0, \qquad (17)$$

becomes much smaller than the core penetration effect and vanishes in the high-ℓ limit as θ converges to $\pi/4$ [Eq. (4)]. The orbital wave functions of the singlet and triplet states become nearly identical except for the exchange symmetry. On the other hand, the coupling between the $j = \ell \pm 1/2$
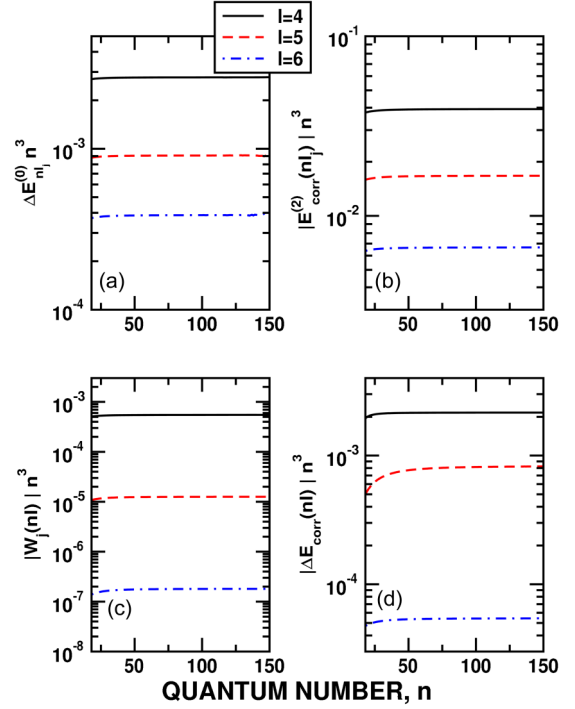

FIG. 3. Calculated scaled energy shift (a) from the hydrogenic energy $n^3 \Delta E_{n\ell_j}^{(0)}$ and (b) due to the correlation effect $n^3 E_{\text{corr}}^{(2)}(n\ell_j)$ [$j = \ell - 1/2$ for both (a) and (b)]. (c) Coupling strength $n^3 |W_j(n\ell)|$ between $j = \ell \pm 1/2$ states and (d) the enhanced magnetic fine structure $n^3 \Delta E_{\text{corr}}(n\ell)$. The energy is in atomic units scaled by n^3.

states [Fig. 3(c)],

$$W_j(n\ell) = {}_0\langle(5s_{1/2}n\ell_{\ell+1/2})JM_J|U_{k=\ell}|(5s_{1/2}n\ell_{\ell-1/2})JM_J\rangle_0, \qquad (18)$$

can become comparable to the spin-orbit splitting between the pair

$$\Delta E_{\text{so}}^{(0)}(n\ell) = E_{5sn\ell_{\ell-1/2}}^{(0)} - E_{5sn\ell_{\ell+1/2}}^{(0)} \qquad (19)$$

for intermediate values of ℓ. The spin-orbit splitting between the unperturbed pair is small but is enlarged by the dynamical polarization of the valence electron by the Rydberg electron. To second order, this correlation effect [Fig. 3(b)] is given by

$$E_{\text{corr}}^{(2)}(n\ell_j)$$
$$= \sum_{\substack{\text{virtual} \\ \text{excitations}}} \sum_k \frac{|{}_0\langle(n_v\ell_{v,j_v}n_R\ell_{R,j_R})JM_J|U_k|(5s_{1/2}n\ell_j)JM_J\rangle_0|^2}{E_{5sn\ell_j}^{(0)} - E_{n_1\ell_{1j_1}n_2\ell_{2j_2}}^{(0)}}, \qquad (20)$$

where the summation extends over k and all virtual excitations of the valence electrons. We note that, in practice, we evaluate numerically Eq. (20) including all contributing multipoles but only considering a selected set of configurations with the valence electron in the $5p$ and $4d$ levels. For the leading terms $k = 1$ and 2, Eq. (20) yields effective dipole and quadrupole polarizabilities and energy corrections approximately proportional to $\langle r^{-4}\rangle$ in analogy to Eq. (6) enhanced, however, by virtual valence excitations. For alkaline-earth-like atoms the

weak correlation between the core and the Rydberg electron leads thus to an indirect coupling between the spin of the core electron and the Rydberg orbital angular momentum complementing the direct magnetic coupling [last term in Eq. (13)]. For strontium this indirect coupling dominates over the direct coupling and enhances the magnetic fine structure increasing the spin-orbit splitting

$$\Delta E_{so}(n\ell) = \Delta E_{so}^{(0)}(n\ell) + \Delta E_{corr}(n\ell), \quad (21)$$

by

$$\Delta E_{corr}(n\ell) = E_{corr}^{(2)}(n\ell_{\ell+1/2}) - E_{corr}^{(2)}(n\ell_{\ell-1/2}) \quad (22)$$

[Fig. 3(d)]. We note that the present results for the energy splitting $\Delta E_{corr}(n\ell)$ are only order-of-magnitude estimates and a more accurate determination would require the inclusion of the coupling to a large number of virtual excitations.

The polarization of the valence electron by the Rydberg electron [Eq. (20)] also provides the leading contribution to the electron-electron interaction term in the quantum defect [Eq. (14)], i.e., $\Delta E_{ee} \simeq E_{corr}^{(2)}(n\ell_j)$. For large $\ell \geqslant 5$, the energy splitting $\Delta E_{corr}(n\ell)$ [Eq. (22)] enhancing the spin-orbit splitting dominates over the coupling $W_j(n\ell)$ between different j. Therefore, the Rydberg states are well represented by the jj-coupling scheme. For $\ell = 4$ the coupling strength $W_j(n\ell)$ becomes comparable to the energy splitting $\Delta E_{corr}(n\ell)$ signaling the onset of the transition to LS coupling. Indeed, a nonperturbative calculation of energy levels by diagonalizing the Hamiltonian [Eq. (11)] yields "singlet" $5sng\,^1G_4$ states with an $\sim$10% admixture of triplet $5sng\,^3G_4$ states and vice versa. Note that, for simplicity, in the following $5sng$ states, which lie between the LS- and jj-coupling schemes, will be denoted by their jj-coupling designation analogous to higher-ℓ states (i.e., "singlet" states $5sng\,^1G_4$ by $5s_{1/2}ng_{9/2}$ and "triplet" states $5sng\,^3G_4$ by $5s_{1/2}ng_{7/2}$). The dominance of $W_j(n\ell)$ becomes increasingly prominent for lower-ℓ states, $\ell \leqslant 3$, and the coupling between the singlet and the triplet states is negligible for most states, i.e., $\theta \to 0$ in Eq. (4).

In the present study, the high-ℓ Rydberg states are excited from the singlet $5snf\,^1F_3$ states to both the $5s_{1/2}n'\ell_{j\pm1/2}$ states by a microwave field. For higher-ℓ states ($\ell > 4$) the $5s_{1/2}n\ell_j$ states are an admixture of the singlet and triplet $5sn\ell$ states [Eq. (4)], each of which is with a weight of approximately 50%. The energy shift [Fig. 3(b)] and the splitting between $j = \ell \pm 1/2$ states are compared with the available data from the present study and from a previous study at lower n ($\sim$20) [16].

IV. RESULTS AND DISCUSSION

A. Quantum defects of F states

Because the high-ℓ states ($\ell > 3$) are excited from an adjacent $5snf\,^1F_3$ state using microwaves, determination of the quantum defect for the high-ℓ states requires knowledge of the ionization energy or quantum defect for the initial F state. Typically the quantum defects of states at high n are extrapolated from measurements at lower n using the Rydberg-Ritz formula

$$\delta = \delta_0 + \frac{\alpha}{(n-\delta_0)^2} + \frac{\beta}{(n-\delta_0)^4} \quad (23)$$

TABLE I. Parameters δ_0, α, and β for use in Eq. (23) taken from Ref. [18].

Series	δ_0	α	β
$5sns\,^1S_0$	3.26896(2)	$-0.138(7)$	0.9(6)
$5snp\,^1P_1$	2.7295(7)	$-4.67(4)$	$-157(2)$
$5snd\,^1D_2$	2.3807(2)	$-39.41(6)$	$-109(2) \times 10^1$
$5snf\,^1F_3$	0.089(1)	$-2.0(2)$	$3(2) \times 10^1$
$5snf\,^1F_3{}^a$	0.0860(1)	$-1.375(2)$	$-7.81(3)$

ᵃRevised values for the present fit to the $^1F_3$ data.

(see Table I for the parameters for various low-ℓ states [18]). The parameters for α and β are the analogs to the $\mu_{2,4}$ [Eq. (10)] derived for high-ℓ alkali-metal atoms. The expansion of Eq. (23) reveals the presence of the terms with odd powers in n (e.g., μ_3/n^3) resulting from the higher-order energy corrections associated with the core polarization potential [28]. These additional odd power terms in Eq. (23), however, are only non-negligible for low-ℓ states. In previous studies the Rydberg-Ritz fitting parameters for the $^1F_3$ states were derived from measurements at $n \lesssim 25$. Since the present results are referenced to $^1F_3$ levels, a series of measurements were first undertaken to test the reliability of the $^1F_3$ Rydberg-Ritz parameters at higher n. In these tests microwave spectroscopy was used to measure the energy spacings between a number of initial $n\,^1F_3$ levels and nearby $^1D_2$ levels as well as between initial $n\,^1P_1$ levels and nearby $^1F_3$ levels (via two-photon absorption). We note that the Rydberg-Ritz fitting parameters for the $^1D_2$ levels were recently tested up to $n \sim 98$ [19,29] and are reliable up to the order of 0.001 in δ.

The present measured energy spacings are presented in Table II together with the values of the quantum defects for the $^1F_3$ states obtained using the extrapolated quantum defects for the $^1P_1$ and $^1D_2$ states. Inspection of Table II shows that the values of the quantum defects predicted based on measurements involving the $^1P_1$ and the $^1D_2$ levels agree to within the uncertainties associated with determining the line centers in the excitation spectra, estimated to be ±1 MHz. The present measured quantum defects do however show a very weak yet consistent n dependence. Nonetheless, the quantum defects measured are very similar to the values $\sim$0.0855 reported in studies at $n \sim 40$ [16]. Such a small change in quantum defect

TABLE II. Measured $^1P_1 \to {}^1F_3$ and $^1F_3 \to {}^1D_2$ energy-level separations and the values of $\delta_0(^1F_3)$ derived from these using the published quantum defects for the $^1P_1$ and $^1D_2$ states (see Table I). The listed uncertainties correspond to an uncertainty of ±1 MHz in determining the line centers.

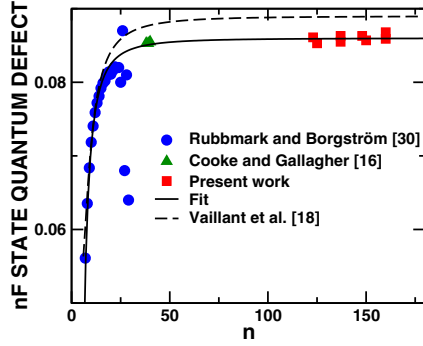| Transition	Measured level separation (MHz)	$\delta_0(^1F_3)$
$125\,^1P_1 \to 125\,^1F_3$	9216.5	0.0853(6)
$137\,^1P_1 \to 137\,^1F_3$	6979.0	0.0855(8)
$150\,^1P_1 \to 150\,^1F_3$	5302.5	0.0857(10)
$160\,^1P_1 \to 160\,^1F_3$	4361.0	0.0859(12)
$123\,^1F_3 \to 126\,^1D_2$	2486.8	0.0861(3)
$137\,^1F_3 \to 141\,^1D_2$	4297.0	0.0863(4)
$148\,^1F_3 \to 152\,^1D_2$	3412.0	0.0863(5)
$160\,^1F_3 \to 164\,^1D_2$	2704.0	0.0868(6)

FIG. 4. The n dependence of the quantum defects for strontium $5snf$ $^1F_3$ states. The figure includes the results of the present measurements (■) together with the earlier measurements of Rubbmark and Borgström [30] (●) and Cooke and Gallagher [16] (▲). The dashed line shows the values predicted using the Rydberg-Ritz formula and the earlier published parameter values in Table I. The solid line is the fit obtained using the revised parameters in Table I. The size of data points encompasses the uncertainty in the measured data.

over a wide range in n implies that the quantum defect converges beyond $n \sim 40$ (Fig. 4). The average of the measured quantum defects for $123 \leqslant n \leqslant 160$ is therefore considered as the converged asymptotic value, $\delta_0(^1F_3) = 0.0860$ with a systematic uncertainty of ~ 0.001 (or less) associated with the uncertainties inherent in the extrapolated quantum defects for the $^1P_1$ and $^1D_2$ states. This value is somewhat lower than the value of $\delta_0 = 0.089$ derived using the low-n data [18]. The solid line in Fig. 4 shows a fit to the available data. The asymptotic value δ_0 is set to the measured average and only α and β are adjusted to obtain the optimal fit. The updated parameters are included in Table I. The fitted parameters deviate strongly from those estimated by Eq. (9) using the polarizabilities of the valence electron clearly indicating the importance of the penetration of the valence shell and the Rydberg–valence electron correlation.

B. Quantum defects of G, H, and I states

We determine the quantum defects for strontium $5sng$ and $5snh$ states in the high-n limit through direct spectroscopic measurements of transitions between initial $5snf$ $^1F_3$ levels and neighboring $5s(n \pm 1)g$ and $5s(n \pm 2)h$ states driven by one- and two-photon processes, respectively. The initial $^1F_3$ levels were excited directly using a 0.5-μs-long 461-nm pulse. Following excitation, the microwave drive was applied for a period of 1 μs. Figure 5 shows typical microwave excitation spectra obtained when driving $5s137f$ $^1F_3 \rightarrow 5s_{1/2}138g_j$ and $5s_{1/2}136g_j$ transitions using low microwave drive voltage amplitudes V_0. Even though the singlet-triplet mixing is weak for $5sng$ states, two distinct features can be resolved in each spectrum. Single-photon excitation from an F state can lead to population of $5s_{1/2}ng_{9/2}$ states, which are predominantly singlet states, and $5s_{1/2}ng_{7/2}$ states, which are predominantly triplet states with a small admixture of singlet states. Each state contributes to the excitation spectrum which can be well fit by the sum of two Lorentzians, each with linewidths of ~ 1 MHz limited by transform broadening. (Tests revealed that small increases in the microwave drive voltage did not
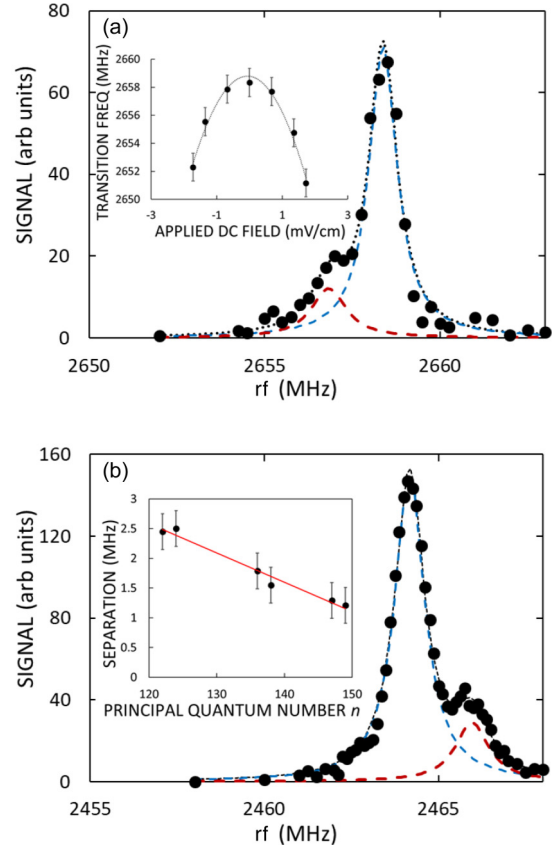

FIG. 5. Microwave spectra observed when driving $5s137f$ $^1F_3$ to (a) $5s_{1/2}138g_j$ and (b) $5s_{1/2}136g_j$ states with microwave drive voltage amplitudes of 160 μV. The solid lines show fits to the measured data obtained using the sum of the two Lorentzians indicated (see the text). The inset in (a) shows the measured shifts in the $5s137f$ $^1F_3$ to $5s_{1/2}138g_j$ transition frequency as a function of a DC field applied along the z axis. The dashed line shows a parabolic fit to the data. The inset in (b) shows the n dependence of the separation in energy between the $5sng_{7/2}$ and $5sng_{9/2}$ states.

change the line positions, indicating that for the range of drive voltage amplitudes used here AC Stark shifts are negligible.) The n dependence of their separations is shown in the inset in Fig. 5(b) and in Fig. 6. The splittings were also calculated nonperturbatively by diagonalizing the Hamiltonian [Eq. (11)]. As shown in Fig. 6, the measured energy splittings ($\sim 0.0008/n^3$) are smaller than the theoretical predictions. This discrepancy is due to the accuracy of the model potential of the core, which only yields quantum defects to an accuracy of the order of 0.01. A similar discrepancy is also seen when comparing to two independent measurements at lower n [13] (see Fig. 6). Measurements at both high and low n follow the same n^{-3} scaling. Narrow excitation features were also obtained when driving two-photon transitions to the $5s_{1/2}nh_{9/2}$ and $5s_{1/2}nh_{11/2}$ levels, although their energy separation, estimated to be ~ 300 kHz at $n \sim 137$ (Fig. 6), was too small to allow their separate resolution. Using the value $\delta_0(^1F_3) = 0.0860$, the measured energy intervals can be converted to quantum defects for the $5s_{1/2}ng_j$ and $5s_{1/2}nh_j$ states (see Fig. 7 and Table III). We again assume that the quantum defects are converged beyond $n > 100$ and
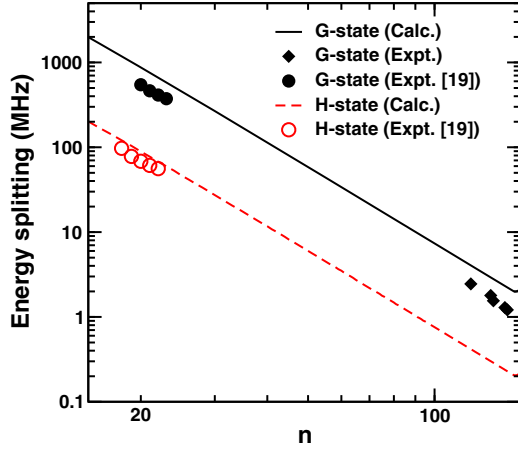
FIG. 6. Measured and calculated splitting of the $j = \ell - 1/2$ and $\ell + 1/2$ states for $\ell = 4, 5$. The solid and dashed lines are the calculated energy splittings. The uncertainty of the measured data is about ± 300 kHz (see Fig. 5). The open and closed circles are the data from [13] and the rhombi are the data from the present study.

the asymptotic values of their quantum defects are taken to be the average over high-n levels yielding $\delta_0(5sng_{7/2}) = 0.0378$, $\delta_0(5sng_{9/2}) = 0.0371$, and $\delta_0(5snh) = 0.0130$. The solid line in Fig. 7 indicates the prediction [Eq. (6)]. The expectation values $\langle r^{-k} \rangle$ are calculated using the eigenstates of the unperturbed Hamiltonian [Eq. (12)] including the effects of the nonhydrogenic core and are found to be nearly independent of
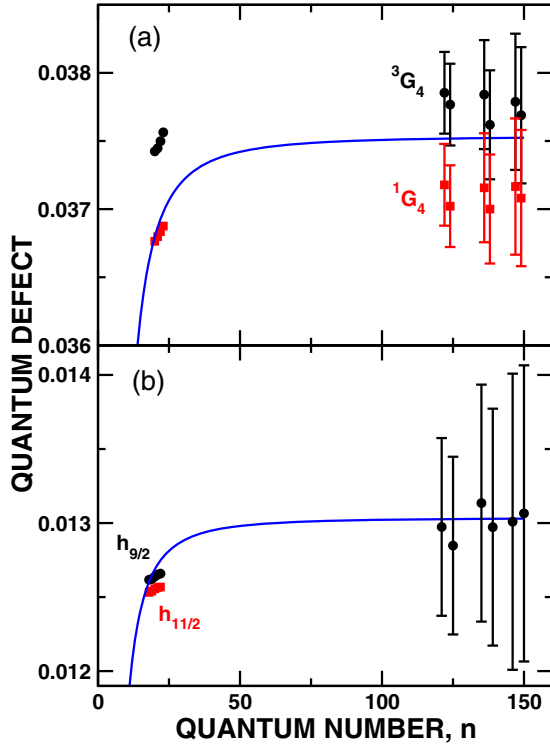

FIG. 7. Measured quantum defects for strontium (a) $5s_{1/2}ng_j$ and (b) $5s_{1/2}nh_j$ states including the results of present measurements for high n (>100) together with the earlier measurements [13] around $n \simeq 20$ (black: $\ell - 1/2$, red : $\ell + 1/2$). The solid blue line is an approximation developed for alkali-metal atoms [Eq. (6)] (see the text for details).

TABLE III. Values of $\delta_0(5sng)$ and $\delta_0(5snh)$ derived from the measured $5snf\,^1F_3 \rightarrow 5sng_j$ and $5snf\,^1F_3 \rightarrow 5snh_j$ energy-level separations using $\delta_0(^1F_3) = 0.0860$ (see the text). The listed uncertainties correspond to an uncertainty of ± 1 MHz in determining the line centers but do not include the systematic error associated with the measurement of $\delta_0(^1F_3)$, which is expected to be $\lesssim 0.001$ (see the text). The representative values included for $n \sim 20$ are derived from energy-level separations reported in [13] and values of $\delta(^1F_3)$ taken from the present best fit to the $^1F_3$ data shown in Fig. 4.

Transition	Measured level separation	$\delta_0(5sng)$ or $\delta_0(5snh)$
$123\,^1F_3 \rightarrow 5s_{1/2}122g_{7/2}$	3412.40 MHz	0.0379 ± 0.0003
$123\,^1F_3 \rightarrow 5s_{1/2}122g_{9/2}$	3409.95 MHz	0.0372 ± 0.0003
$123\,^1F_3 \rightarrow 5s_{1/2}124g_{7/2}$	3666.75 MHz	0.0378 ± 0.0003
$123\,^1F_3 \rightarrow 5s_{1/2}124g_{9/2}$	3669.25 MHz	0.0370 ± 0.0003
$137\,^1F_3 \rightarrow 5s_{1/2}136g_{7/2}$	2465.96 MHz	0.0378 ± 0.0004
$137\,^1F_3 \rightarrow 5s_{1/2}136g_{9/2}$	2464.17 MHz	0.0372 ± 0.0004
$137\,^1F_3 \rightarrow 5s_{1/2}138g_{7/2}$	2656.83 MHz	0.0376 ± 0.0004
$137\,^1F_3 \rightarrow 5s_{1/2}138g_{9/2}$	2658.38 MHz	0.0370 ± 0.0004
$148\,^1F_3 \rightarrow 5s_{1/2}147g_{7/2}$	1954.04 MHz	0.0378 ± 0.0005
$148\,^1F_3 \rightarrow 5s_{1/2}147g_{9/2}$	1952.75 MHz	0.0372 ± 0.0005
$148\,^1F_3 \rightarrow 5s_{1/2}149g_{7/2}$	2108.74 MHz	0.0377 ± 0.0005
$148\,^1F_3 \rightarrow 5s_{1/2}149g_{9/2}$	2109.95 MHz	0.0371 ± 0.0005
$20\,^1F_3 \rightarrow 5s_{1/2}20g_{7/2}$	37.3932 GHz	0.0374
$20\,^1F_3 \rightarrow 5s_{1/2}20g_{9/2}$	37.9388 GHZ	0.0368
$23\,^1F_3 \rightarrow 5s_{1/2}23g_{7/2}$	24.9574 GHz	0.0376
$23\,^1F_3 \rightarrow 5s_{1/2}23g_{9/2}$	25.3310 GHz	0.0369
$123\,^1F_3 \rightarrow 5s121h$	6991.4 MHz	0.0130 ± 0.0006
$123\,^1F_3 \rightarrow 5s125h$	7163.6 MHz	0.0128 ± 0.0006
$137\,^1F_3 \rightarrow 5s135h$	5046.6 MHz	0.0131 ± 0.0008
$137\,^1F_3 \rightarrow 5s139h$	5196.0 MHz	0.0130 ± 0.0008
$148\,^1F_3 \rightarrow 5s146h$	3995.7 MHz	0.0130 ± 0.0010
$148\,^1F_3 \rightarrow 5s150h$	4127.5 MHz	0.0131 ± 0.0010
$18\,^1F_3 \rightarrow 5s_{1/2}18h_{9/2}$	78.4828 GHZ	0.0126
$18\,^1F_3 \rightarrow 5s_{1/2}18h_{11/2}$	78.5800 GHz	0.0125
$22\,^1F_3 \rightarrow 5s_{1/2}22h_{9/2}$	43.8132 GHz	0.0127
$22\,^1F_3 \rightarrow 5s_{1/2}22h_{11/2}$	43.8692 GHz	0.0126

the spin of the Rydberg electron. The effective polarizabilities are chosen as $\alpha_{d,q} = b\alpha_{d,q}^{(0)}$ by multiplying a constant factor b to the (static) polarizabilities ($\alpha_d^{(0)} = 86$ and $\alpha_q^{(0)} = 100$ [13]). For the best fit $b = 0.875$ is chosen for $5sng$ states and $b = 0.925$ for $5snh$ states. The smaller value of b for $5sng$ states implies larger corrections due to the dynamical polarization and the magnetic fine structure. We note that a more accurate evaluation of the effective quadrupole polarizability requires data for lower-n levels where the expectation value $\langle r^{-6} \rangle$ becomes more dominant.

Attempts were also made to measure the quantum defects for high-n $5sni$ states by observing two-photon transitions from initial $5sng$ levels. This proved challenging because the SFI spectra for the $5sng$ and $5sni$ states were rather similar, rendering it difficult to identify transitions between such states. Nonetheless, transitions from the $5s137g$ and $5s139g$ initial levels were identified and analysis of the data (not including the systematic uncertainty) yielded the value $\delta_0(5sni) = 0.0051 \pm 0.0010$, which is consistent with the value $\delta_0 \simeq 0.0058$ deduced from the earlier measurements at $n \sim 20$ [13].

High-n Rydberg energy levels, however, are sensitive to the presence of small stray electric fields. To test for the presence of systematic errors associated with the possible presence of such fields, measurements of the $5s137f\,^1F_3 \rightarrow 5s138g_j$ transition were undertaken first with the stray fields minimized as in our earlier studies [21] and then with additional offset potentials applied to opposing pairs of the electrodes that surround the excitation region to generate weak, but known, DC electric fields. The effects of such fields on the transition frequency are shown in the inset in Fig. 5(a) for DC fields applied in the vertical (z) direction. Similar behavior was seen for fields applied in the x and y directions. In all cases the data could be well fit by a parabola symmetric about zero applied offset field, confirming that the deviation is due to the quadratic Stark effect and that stray fields have been reduced to a very small value. Interestingly, at $n = 137$ the presence of stray fields as large as $\pm 700\ \mu\text{V cm}^{-1}$, which are more than an order of magnitude larger than the precision with which we can zero the electric field, generate line shifts of only $\sim \pm 1$ MHz.

V. CONCLUSIONS

The present work provides measurements of the quantum defects δ for the higher-ℓ strontium Rydberg states in the high-n limit. The ℓ dependence of the quantum defects reflects the transition from an LS-coupling regime, $\ell \lesssim 4$, where penetration of the valence shell by the Rydberg electron and the exchange term of the electron-electron interaction dominates, to the jj coupling regime for $\ell \geqslant 5$ where the magnetic fine structure enhanced by dynamical polarization effects prevails. For the $\ell = 4$ transition states, the electron-electron interaction is still dominant, but mixing between singlet and triplet states is clearly detectable. The present work also attests to the reliability of the previously derived Rydberg-Ritz parameters for the $^1P_1$ and $^1D_2$ states in the high-n limit. Furthermore, the present work demonstrates that direct production of high-n strontium $5sng_j$ and $5snh_j$ Rydberg states can be achieved through combined multiphoton microwave-optical excitation. Such high-ℓ states provide new opportunities for the study of novel ultralong-range Rydberg molecules and of autoionization.

[1] M. T. Eiles, J. Phys. B **52**, 113001 (2019).

[2] C. H. Greene, A. S. Dickinson, and H. R. Sadeghpour, Phys. Rev. Lett. **85**, 2458 (2000).

[3] J. Tallant, S. T. Rittenhouse, D. Booth, H. R. Sadeghpour, and J. P. Shaffer, Phys. Rev. Lett. **109**, 173202 (2012).

[4] T. K. Langin, G. M. Gorman, and T. C. Killian, Science **363**, 61 (2019).

[5] D. A. Tate and T. F. Gallagher, Phys. Rev. A **97**, 033410 (2018).

[6] I. C. Percival, Proc. R. Soc. London Ser. A **353**, 289 (1977).

[7] U. Eichmann, V. Lange, and W. Sandner, Phys. Rev. Lett. **68**, 21 (1992).

[8] M. Seng, M. Halka, K.-D. Heber, and W. Sandner, Phys. Rev. Lett. **74**, 3344 (1995).

[9] G. Tanner, K. Richter, and J.-M. Rost, Rev. Mod. Phys. **72**, 497 (2000).

[10] E. A. Hessels, W. G. Sturrus, S. R. Lundeen, and D. R. Cok, Phys. Rev. A **35**, 4489 (1987).

[11] T. F. Gallagher, R. Kachru, and N. H. Tran, Phys. Rev. A **26**, 2611 (1982).

[12] R. A. Komara, M. A. Gearba, S. R. Lundeen, and C. W. Fehrenbach, Phys. Rev. A **67**, 062502 (2003).

[13] J. Nunkaew, E. S. Shuman, and T. F. Gallagher, Phys. Rev. A **79**, 054501 (2009).

[14] E. L. Snow, R. A. Komara, M. A. Gearba, and S. R. Lundeen, Phys. Rev. A **68**, 022510 (2003).

[15] R. R. Freeman and D. Kleppner, Phys. Rev. A **14**, 1614 (1976).

[16] W. E. Cooke and T. F. Gallagher, Opt. Lett. **4**, 173 (1979).

[17] R. Ito, K. Tsurui, T. Sugawara, Y. Kazama, K. Kitano, and H. Maeda, in *2018 43rd International Conference on Infrared,* *Millimeter, and Terahertz Waves (IRMMW-THz), Nagoya, 2018* (IEEE, Piscataway, 2018), p. 574.

[18] C. L. Vaillant, M. P. A. Jones, and R. M. Potvliege, J. Phys. B **45**, 135004 (2012).

[19] R. Ding, J. D. Whalen, S. K. Kanungo, T. C. Killian, F. B. Dunning, S. Yoshida, and J. Burgdörfer, Phys. Rev. A **98**, 042505 (2018).

[20] G. Fields, F. B. Dunning, S. Yoshida, and J. Burgdörfer, Phys. Rev. A **99**, 022710 (2019).

[21] M. T. Frey, X. Ling, B. G. Lindsay, K. A. Smith, and F. B. Dunning, Rev. Sci. Instrum. **64**, 3649 (1993).

[22] R. F. Stebbings and F. B. Dunning, *Rydberg States of Atoms and Molecules* (Cambridge University Press, Cambridge, 1983).

[23] T. F. Gallagher, *Rydberg Atoms* (Cambridge University Press, New York, 1994).

[24] H. A. Bethe and E. E. Salpeter, *Quantum Mechanics of One- and Two-Electron Atoms* (Plenum, New York, 1977).

[25] S. Ye, X. Zhang, F. B. Dunning, S. Yoshida, M. Hiller, and J. Burgdörfer, Phys. Rev. A **90**, 013401 (2014).

[26] G. Fields, X. Zhang, F. B. Dunning, S. Yoshida, and J. Burgdörfer, Phys. Rev. A **97**, 013429 (2018).

[27] A. Messiah, *Quantum Mechanics* (North-Holland, New York, 1970), Vol. 2.

[28] G. W. F. Drake and R. A. Swainson, Phys. Rev. A **44**, 5448 (1991).

[29] R. Ding, Ph.D. thesis, Rice University, 2019.

[30] J. R. Rubbmark and S. A. Borgström, Phys. Scr. **18**, 196 (1978).